

Review

## Analysis of landing site attributes for future missions targeting the rim of the lunar South Pole Aitken basin

David Koebel\*, Michele Bonerba, Daniel Behrenwaldt, Matthias Wieser, Carsten Borowy

OHB-System AG, Germany, Karl-Ferdinand-Braun-Straße 8, D-28359 Bremen, Bremen, Germany

### ARTICLE INFO

*Article history:*

Received 20 January 2011

Received in revised form

14 February 2012

Accepted 9 March 2012

Available online 9 August 2012

*Keywords:*

Moon

South Pole

Photovoltaic

Illumination map

Kaguya digital elevation map

### ABSTRACT

For the South polar lunar region between  $-85$  and  $-90^\circ$  Latitude an updated analyses of the solar illumination and ground station visibility conditions has been performed in the frame of a feasibility study for an ESA Lunar Lander mission. The analyses are based on the refined lunar digital elevation model provided by the Japanese Kaguya/Selene mission, originating from its LASER altimeter instrument. For the South polar region maps of integral solar illumination are presented for a mission epoch in 2016. The analysis modelling was validated with the help of a Kaguya High Definition video. The solar illumination is driving for the power subsystems of any robotic lander craft or manned lunar outpost, in case they rely on conventional photovoltaic power generation with battery buffering of shadowed periods. In addition the visibility of the terrain from a terrestrial ESA ground station was analysed. The results are presented as an integral ground contact duration map, being crucial for the operations of any lunar outpost. Considering these two quality criteria, several possible landing sites for a future lunar mission have been pre-selected. For these sites a detailed analysis of quasi-continuous illumination conditions is presented. This includes magnified maps of the pre-selected areas, showing any location's longest illumination intervals that are allowed to be interrupted by shadows with limited duration only. As a final quality criterion, the terrain topology has been analysed for its impact on the landing trajectory. From a trade-off between the three quality criteria the connecting ridge between the Shackleton and the de Gerlache was determined to provide the most favourable landing site quality. This site is located at  $89^\circ 28' \text{ South}$ ,  $136^\circ 40' \text{ West}$ , and 1947 m altitude, and features an integral illumination of 85.7%. With battery energy to sustain shadows of 120 h, total mission duration of 9.37 sidereal months can be guaranteed.

© 2012 Elsevier Ltd. All rights reserved.

**Abbreviations:** ARCGIS, Aeronautical Reconnaissance Coverage Geographic Information System; ASCII, American Standard Code for Information Interchange; DEM, Digital Elevation Model; DSA, Deep Space Antenna; ENVI, Environment for Visualising Images; ESA, European Space Agency; ESOC, European Space Operations Centre; ESTEC, European Space Technology Centre; GIS, Geographic Information System; GNC, Guidance, Navigation, and Control; G/S, Ground Station; HD, High Definition; ISIS, Integrated Software for Imagers and Spectrometers; LASER, Light Amplification by Stimulated Emission of Radiation; LCROSS, Lunar CRater Observation and Sensing Satellite; LRO, Lunar Reconnaissance Orbiter; N/A, Not Applicable; NASA, National Aeronautics and Space Administration; OBDDH, On-Board Data Handling; PDS, Planetary Data System; PEL, Peaks of Eternal Light; RADAR, Radio Detection And Ranging; RHU, Radioisotope Heater Units; RTG, Radioisotope Thermoelectric Generators; SPA, South Pole Aitken; STK, Satellite Tool Kit; TBC, to be confirmed; TBD, to be defined; TMTC, Telemetry and Tele-Control; USGS, United States Geological Survey; UTCG, Universal Time Coordinate Gregorian

\* Corresponding author. Tel.: +49 0 421 2020 790; fax: +49 0 421 2020 700.

E-mail addresses: [david.koebel@nord-com.net](mailto:david.koebel@nord-com.net), [david.koebel@ohb-system.de](mailto:david.koebel@ohb-system.de) (D. Koebel), [michele.bonerba@ohb-system.de](mailto:michele.bonerba@ohb-system.de) (M. Bonerba), [daniel.behrenwaldt@ohb-system.de](mailto:daniel.behrenwaldt@ohb-system.de) (D. Behrenwaldt), [matthias.wieser@ohb-system.de](mailto:matthias.wieser@ohb-system.de) (M. Wieser), [carsten.borowy@ohb-system.de](mailto:carsten.borowy@ohb-system.de) (C. Borowy).

## Contents

|      |  |     |
|------|--|-----|
| 1.   | Requirements and rationale . . . . .                                     | 198 |
| 1.1. | Introduction . . . . .   | 198 |
| 1.2. | Preceding analyses . . . . .   | 199 |
| 2.   | Analysis processes and tools set-up . . . . .                            | 199 |
| 2.1. | Topography of the peaks of eternal light . . . . .                       | 199 |
| 2.2. | Illumination and ground contact analyses approach . . . . .              | 200 |
| 2.3. | Lunar digital elevation models and the South Pole Aitken basin . . . . . | 201 |
| 3.   | Illumination and ground contact analyses and results . . . . .           | 202 |
| 3.1. | Integral annual terrain illumination . . . . .                           | 202 |
| 3.2. | Integral annual ground contact percentage map . . . . .                  | 203 |
| 3.3. | Selection of candidate landing sites . . . . .                           | 203 |
| 3.4. | Detailed illumination and ground contact timeline analyses . . . . .     | 204 |
| 3.5. | Illumination gaps analysis . . . . .                                     | 206 |
| 4.   | Verification and error analysis . . . . .                                | 211 |
| 4.1. | Comparison of simulation and remote sensing imagery . . . . .            | 211 |
| 4.2. | Comparison of analysis results . . . . .                                 | 211 |
| 4.3. | Error estimation . . . . .   | 213 |
| 5.   | Conclusions . . . . .  | 214 |
|      | References . . . . .   | 215 |

## 1. Requirements and rationale

### 1.1. Introduction

The lunar South polar region is of high scientific interest and in many aspects advantageous for any exploration mission. The polar terrain is located at the rim of the Aitken Basin, being the largest known impact crater in the solar system.

The celestial configuration of the Moon and the Earth is depicted in Fig. 1. Earth polar axis is inclined by  $23.5^\circ$  and precesses with a period of approximately 25,000 years. The Moon's polar axis is inclined only about  $1.54^\circ$ . Despite the  $5^\circ$  inclination of its orbit plane and the 18 years periodic precession of its polar axis and orbit plane, sunlight is always nearly horizontal at the lunar poles [1].

Polar areas are always either dark or at grazing solar incidence with intermittent shadowing. For a planetary station at the lunar pole the Sun seems to rotate during one lunar day or one sidereal month around  $360^\circ$  azimuth. The solar elevation is dependent upon the lunar seasons, with solstices of  $-1.54^\circ$  during lunar winter, and  $+1.54^\circ$  during lunar summer. There thus exist mountain peaks that are characterised by near eternal illumination, which provide a benign thermal environment for any long-term robotic or manned lander mission and ideal conditions for photovoltaic power generation. Sunlit polar surfaces feature moderate temperature variations of  $-10^\circ \pm 50^\circ\text{C}$  [2].

In contrast to this, depressed polar surfaces, like crater grounds, lie in near-permanent darkness, and are thus very cold. Uncertainties in lunar heat flow values [3] suggest that the temperatures within these cold traps vary between 50 and 70 K. At these temperatures, atoms and molecules of volatile species cannot escape [4]. The smaller impact craters in the polar region are therefore believed to harbour water resources that remain conserved through the cryogenic temperatures inside them. The ice would originate from the bombardment of comets throughout the billions of years after the formation of the lunar crust.

A renewed international interest in lunar exploration could be observed during the last decade. The derived missions firstly are remote-sensing orbiters and secondly will be lander missions. Some general motivations for a polar lunar lander mission are technology demonstration and preparatory activities for permanent lunar bases.

There exists a particular scientific interest in the exploration of the South Pole Aitken (SPA) Basin, from which geologists expect evidence on the origin of the Earth–Moon System. This is due to the belief that material from the lunar mantle may have been ejected to the surface (see [2,5,6]) by the giant impact, from which it originates. As key information this material may or may not feature geologic properties similar to minerals found

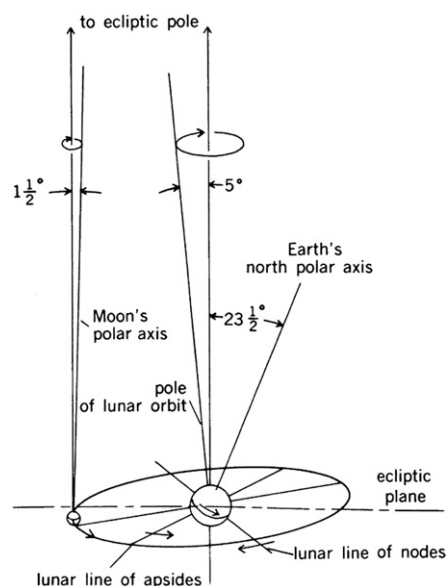


**Fig. 1.** Moon and Earth celestial configuration (reprinted from [1]).

on Earth. The analysis of volatiles within the permanently shadowed craters is of importance for exobiology, because of possible incubators within the comet ice remnants [7].

The in-situ utilisation of water resources, on the other hand, is an essential prerequisite for extended human subsistence within a lunar base. This is due to the associated mission cost reductions that are anticipated when resources for the life support system need not be brought along. Oxygen is essential for breathable air, and hydrogen and oxygen can be used as a rocket propellant.

The presented results are derived from associated work on a robotic lunar lander mission, of which OHB-System has been studying the feasibility for the European Space Agency [8]. The mission will perform a landing with pinpoint precision within the South polar area. The driving requirement for the power subsystem of the lander craft was the use of photovoltaic power. Any use of Radioisotope Thermoelectric Generators (RTG) for power generation or Radioisotope Heater Units (RHU) for thermal control was forbidden by the customer [9]. This is due to the hazards associated with launching radioactive material. In order to determine the optimum landing location, detailed analyses of illumination and ground contact conditions were carried out and associated maps for the entire area were generated.

## 1.2. Preceding analyses

There have been several publications on analyses of possible landing sites at the lunar South Pole, which aimed at the existence and solar illumination conditions of the so-called peaks of eternal light.

In the frame of the ESA-study Euromoon 2000 Kruijff and Michiel [10] conducted an illumination analysis with topographic modelling derived from the Clementine data. A 3D topography model of the lunar South Pole was generated from an analysis of the visible imagery and from a RADAR image generated by the Arecibo observatory. As the data coverage was limited to the lunar Southern winter, both extent and accuracy of the analysis was limited. The integral annual illumination was not calculated, for which reason a direct comparison of results is not possible.

An extensive review and update of the illumination analyses for the lunar south polar terrain was performed in 2007 by Fincannon [11] on the basis of a digital elevation model derived from Goldstone Solar System RADAR data. In [11] an analysis tool was developed for the assessment of most locations near the lunar Poles. Average illumination fractions, energy storage duration, solar terrain elevation profiles above the horizon and illumination fraction profiles were presented for various highly illuminated sites. The aim of this work was to provide the power system engineer of any manned or unmanned lander craft with a quantitative design tool chain.

An illumination map of the lunar South Pole based on Kaguya Digital Elevation Model (DEM) was generated in 2009 by McClanahan [12]. The aim of this analysis was to detect permanently shadowed craters for the Lunar CRater Observing and Sensing Satellite (LCROSS) mission of NASA.

The sunlit conditions of the lunar polar region were estimated by Noda et al. [13], on the basis of the digital elevation model made from the Laser altimeter data of Kaguya. The reported integral illumination maps generated for the South polar region matched qualitatively and quantitatively with the present analysis results, with detected maxima of 86% as compared to 85.71% (see section 3.3).

A comprehensive study of the illumination conditions at the Moon's South Pole was conducted by Bussey et al., also on the basis of Kaguya Laser altimeter-derived topography [14]. Therein a software programme was developed for the precise simulation of the illumination conditions. This was used to calculate illumination maps, but also inversely maps of deepest shadows, that is of least influx of solar illumination or Earth albedo. Additionally, detailed illumination profiles and eclipse analyses were performed.

In 2011 Mazarico et al. [15] used high-resolution altimetry data obtained by the Laser altimeter instrument onboard the Lunar Reconnaissance Orbiter to characterize the present illumination conditions in the polar regions of the Moon. The simulations were carried out with increased spatial and temporal extent, compared to previous studies. Both permanently shadowed regions and illuminated peaks were investigated, because of the importance of those sites for exploration and engineering considerations.

Vanoutryve et al. [9] reported about the analyses of the illumination and communication conditions at the lunar South Pole based on terrain models derived from the Kaguya Laser Altimeter. This work was also focused on the system design of the European Space Agency's Lunar Lander mission. For the most promising locations, the influence of several parameters was assessed, as well as the communication conditions.

Any robotic or manned lunar outpost needs to transmit a telemetry stream of scientific and status data to the ground station, and to receive a tele-command data stream of instruction sets. The quality of the radio link is dependent upon the line-of-sight visibility to the deep space antenna. Thus no generic mappings can be generated and no associated publications are known.

## 2. Analysis processes and tools set-up

### 2.1. Topography of the peaks of eternal light

In [10] the required topographical height restrictions for a peak of eternal light have been determined. Considering the worst case geometrical illumination condition of a lunar attitude, given between midnight to midday at winter solstice, a peak of eternal light can only be found within a radius of 157 km from the pole. A true peak of eternal light however, in the sense of a really permanently lit surface cannot exist, since it would be a conical mountain, 600 m higher than the mean radius of 1737.4 km, with a sharp top angle of less than 177°, and an infinitesimally small surface area.

In a more relaxed scenario, a vertical surface needs to be illuminated instead. This may be given by a lander craft's solar panel that is elevated a certain height  $H$  above the surface. The solar panel can be rotated along a vertical axis around 360° azimuth, so that it always faces in solar

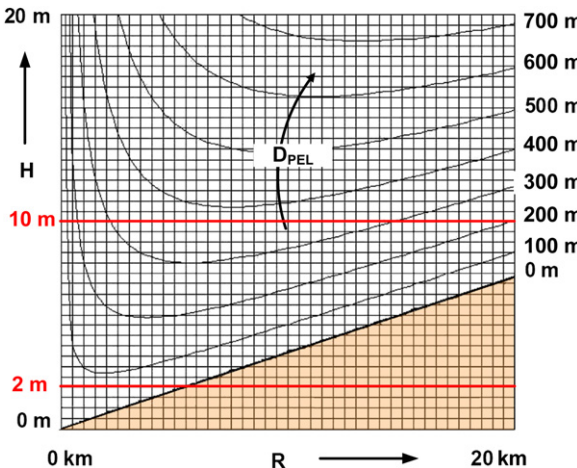


**Fig. 2.** (Colour online) Geometric conditions for eternal illumination (adapted reprint from [10]).

direction. In an idealised approximation, the top of a mountain is assumed to follow a circular curvature with radius  $R$ . Fig. 2, depicts the achievable landing surface diameter  $D_{PEL}$  for perpetual lighting on the solar panels as a function of  $H$  and  $R$ .

In the diagram of Fig. 2 the circular curvature of the mountain top is assigned to the abscissa. Assigned to the ordinate is the height of the solar generator respectively solar power tower  $H$ . The parametric curves indicate the circular landing area diameter on top of the peak of eternal light respectively their dependency on the geometric parameters  $R$  and  $H$ . Within the orange triangular area of the diagram, no peaks of eternal light exist. A peak of eternal light is therefore defined as the area on which a specific planetary lander can receive perpetual sunlight. A height of 2 m above ground of the solar generator has been assumed within the present study. The beneficial effects of solar panels elevated by 10 m above ground and of a solar power tower of 100 m altitude have been considered in [15] and in [11].

## 2.2. Illumination and ground contact analyses approach

Fig. 3 depicts a flowchart of the different processing steps that have been used for the illumination and ground contact analyses within the present analyses. It includes the required pre-processing of ephemerides of Moon, Sun and Earth as an input for the geometry of illumination by either the Sun or the ground station TMTc RADAR beam. The post-processing consists of geometric corrections and superposition of the illumination and ground station access time maps.

Rendering planetary surfaces in detail is challenging [16], because of the enormous amount of data that needs to be processed and because of the large amount of floating point operations required (see [17,18]). The topography dataset of digital elevation grid points for the global lunar terrain denoted a DEM number 1 in Section 2.3 has required some 450 GB of memory.

The following software tools have been used:

- Satellite Tool Kit (STK) and Coverage Module from Analytical Graphics Inc. [19].
- Global Mapper from Global Mapper Software LLC/United States Geological Survey (USGS) as support tool required for the pre- and post-processing of the DEM [20].
- ENVI 4.7 for ArcGIS from ITT Exelis Visual Information Solutions for initial DEM evaluations [21].
- ISIS (Integrated Software for Imagers and Spectrometers) from the USGS for initial DEM evaluations [22].

In the first step of the analysis the Kaguya DEM has been translated in a format compatible to STK. This has been performed by the Global Mapper, a Geographic Information System (GIS), which can be used to read ASCII terrain datasets and generate a Digital Elevation Model (DEM). The Kaguya ASCII datasets have been imported as an “elevation grid”. Every text line contains the three-dimensional polar coordinates of each surface point of the model. The latitude and longitude coordinates are followed by the point elevation relative to the lunar spherical datum, which is the reference sphere of 1737.4 km radius. From these 3D coordinate data a triangulated terrain elevation grid has been generated. The grid has been created using the selected vector data. Once the dataset is loaded, it can be exported in a single file, keeping the original grid within the specified export bounds, and in a format that is compatible with the specifications of the USGS.

In the detailed analysis of the potential landing sites the Digital Elevation Model number 3, as described in Section 2.3, was utilised. Generally, when two different datasets are connected, an edges mismatch at the model borders can appear that is due to deviations in the models, especially because of different spatial resolutions. This mismatch has been corrected by a functionality that does a so-called “feathering” on the area of overlap of two layers. The border of the feathered area has been sized to be equal to 50 pixels.

In the next step of the analysis, the simulation software suite Satellite Tool Kit has been utilised both for calculating the times of Earth station visibility from the lunar Polar Region as well as for the actual illumination analysis. For these purposes, the programme module STK/Coverage has to be used. This module determines inter-visibility or line of sight accesses between the assigned assets and (in our case) a continuous area using a grid of evenly spaced points. For the modelling of the lunar terrain within STK, the altitude for each grid point of the DEM is determined with respect to the Moon reference sphere of 1737.4 km radius. From the terrain data a local horizon for each grid point is calculated, which forms the baseline for the line of sight access computations.

More in detail, each grid point has been characterised as a target with precise constraints applied to line of sight towards the Sun as well as towards the ground station. For the ground station visibility analysis, the line of sight contact times between each grid point and the New Norcia ground station (for details refer to section 3.2) have been analysed. For the illumination analysis, since the Sun cannot be classified by STK as asset within the Coverage Tool, the illumination source has been modelled by two “facilities” at the poles of the Sun. Removing the Sun obstruction between

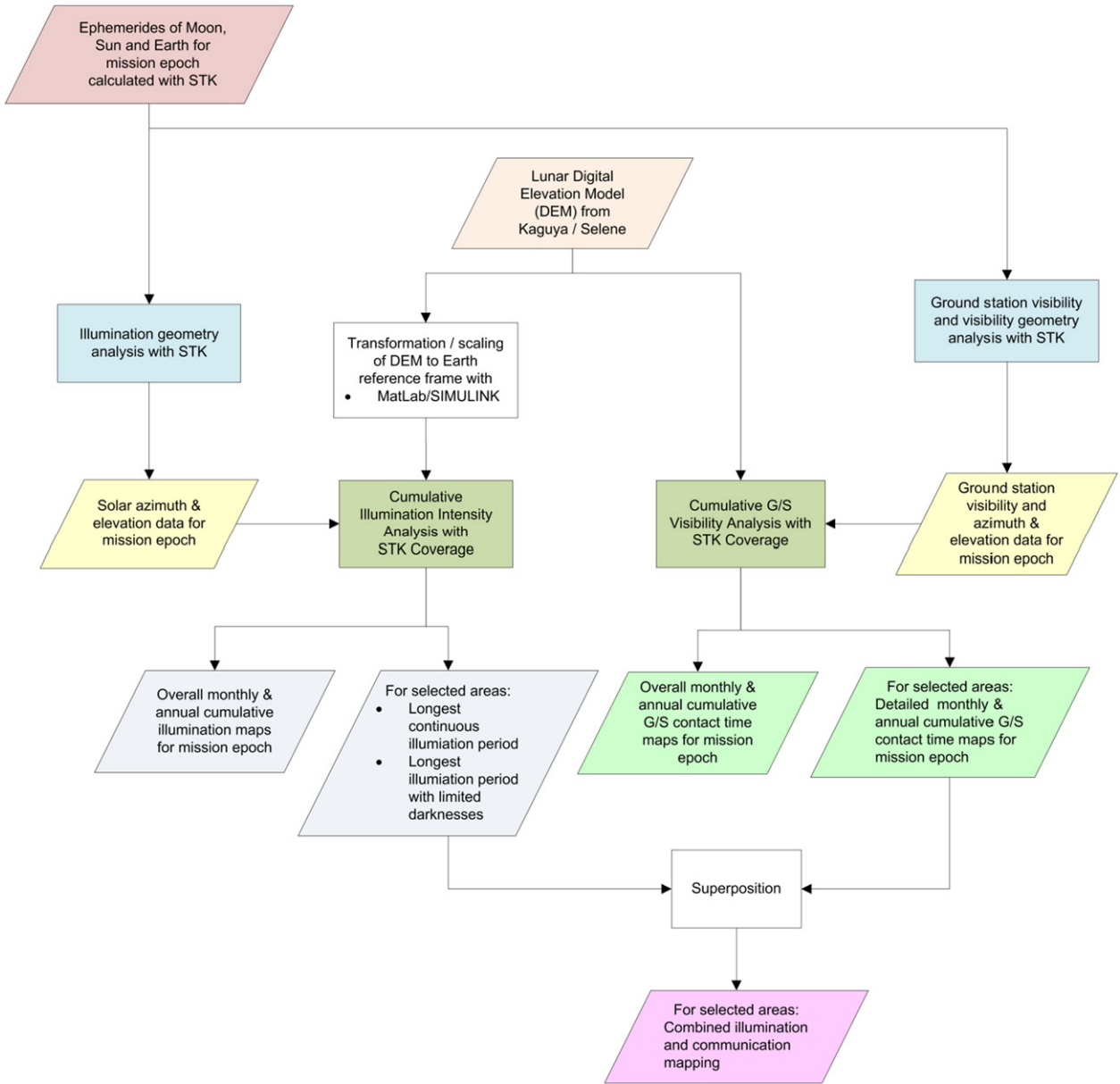


**Fig. 3.** (Colour online) Flowchart of illumination and ground contact analyses including pre- and post-processing.

the facilities and the grid points line of sight, and analysing the contact times between the new Sun asset and the grid points, the overall illumination conditions for the area of interest has been analysed for the mission epoch.

The height of the “ground assets” at the analysed grid points, that is the height of the virtual lander bodies, their solar panel and Earth-pointing antenna, was assumed to be 2 m above the ground.

### 2.3. Lunar digital elevation models and the South Pole Aitken basin

Fig. 4 depicts a model of the southern hemisphere of the lunar relief, wherein the zero meridian is pointing

upwards. This first Digital Elevation Model was generated from the Kaguya global topographic map, which features a polar coordinate grid resolution of  $1/16^\circ$  both in longitude and in latitude, equalling a grid cell area of  $1895 \text{ m} \times 1895 \text{ m}$  at the equator (LALT\_GGT\_NUM of [23], available at [24]). The South Pole Aitken basin is the prominent feature to be distinguished on the lunar far side. This basin features a diameter of 2500 km and variations in altitude as large as 14 km [25].

A second model of the lunar relief was generated as a combination of two Kaguya Digital Elevation Models of different resolutions. The South polar region below  $-85^\circ$  latitude was mapped using the medium-resolution Digital Elevation Model featuring a grid sampling of  $1/64^\circ$  in

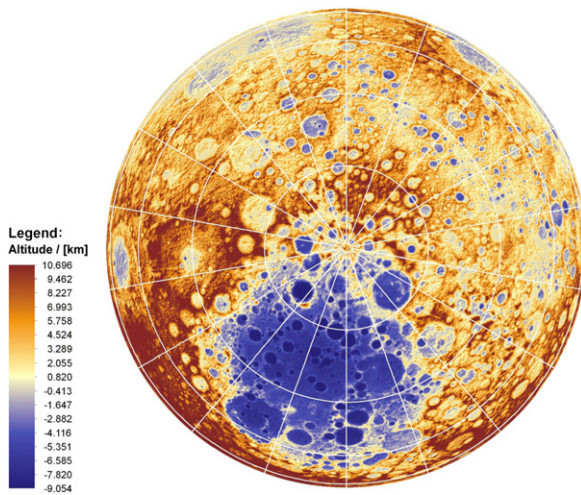


**Fig. 4.** Southern lunar hemisphere altitude relief from Kaguya DEM.

latitude and  $0.179^\circ$  in longitude, which equals a grid cell area of  $474\text{ m} \times 5428\text{ m}$  at the equator (LALT\_SP of [23]). The rest of the global terrain was mapped using the low-resolution Digital Elevation Model with a definition of  $1^\circ$  both in latitude and in longitude.

A third model was generated with the Kaguya high-resolution Digital Elevation Model of the South polar region below  $-85^\circ$  latitude. This DEM featured a grid sampling of  $1/128^\circ$  in latitude and  $1/32^\circ$  in longitude, equalling a grid cell area of  $237\text{ m} \times 948\text{ m}$  at the equator (LALT\_GT\_SP\_NUM of [23]). The rest of the global terrain again was mapped using the low-resolution Digital Elevation Model with a definition of  $1^\circ$  both in latitude and in longitude. This model was utilised for generating Fig. 5, which depicts a close-up view of the Shackleton crater with a line-of-sight in Earth direction. The image was generated with the help of the Satellite Tool Kit software suite, which was used for the detailed analyses described in the following. The artefacts in the model reveal the satellite ground tracks crossing at the South Pole. They are due to the measurement errors, comprising Laser altimeter instrument error and orbit perturbations. Both errors cannot be completely corrected by data post-processing (see section 4.3).

For all models the Global Mapper Geographic Information System was used to read the ASCII terrain dataset and to generate a Digital Elevation Model. This was provided in a data format based on the Planetary Data System (PDS) [23]. All Kaguya models reference the altitude data to a lunar datum sphere of 1737.4 km radius.

The South polar lunar terrain is characterised by variations in altitude that range from heights of 6784 m of the Leibnitz Mountain to depths of  $-4105\text{ m}$  of the nearby Shoemaker Crater. These values were read from the second Digital Elevation Model depicted in Fig. 6, wherein the lunar latitudes between  $-85$  and  $-90^\circ$  are mapped. Landmark craters and mountains are indicated, together with an attempt to indicate the approximate border of the South Pole Aitken Basin. It is probable however, that the Malapert and Leibnitz Mountains themselves are features of the SPA crater rim [25].

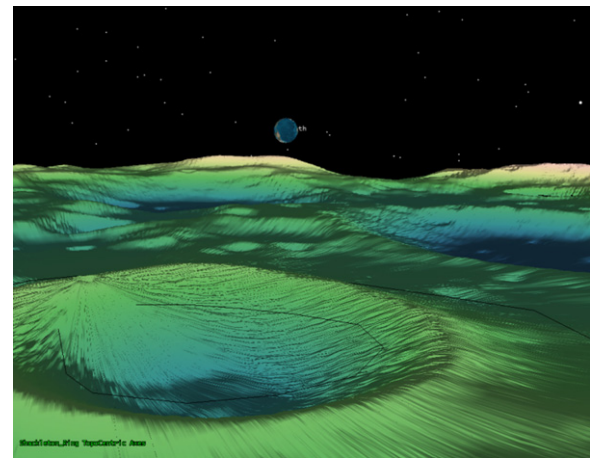


**Fig. 5.** Lunar South Pole at the Shackleton crater and view towards Malapert Mountain and Earth.

Also read from the Digital Elevation Model depicted in Fig. 6 were the approximate circular curvatures of the following mountain ridges and crater rims:

- 0.4 to 0.8 km for the Shackleton and de Gerlache craters.
- 1.9 km for the connecting ridge between Shackleton and de Gerlache craters.
- 1.25 km for the Malapert Mountain.

With these values, with an assumed height of the solar generator of 2 m, and from Fig. 2, which indicates the geometric conditions for eternal illumination, it can be read that the diameter of any peak of eternal light will possess a magnitude of approximately 100 m only.

### 3. Illumination and ground contact analyses and results

#### 3.1. Integral annual terrain illumination

An overall and integral illumination analysis was performed as a starting point for the characterisation of the area of interest and the preliminary selection of candidate landing sites. These were subsequently analysed in more detail in section 3.4.

For the integral illumination analysis the Digital Elevation Model number 2, as described in Section 2.3 was utilised. From this DEM with a grid sampling of  $1/64^\circ$  in latitude and  $0.179^\circ$  in longitude, a STK-model was generated with a triangular mesh of 474 m granularity. The use of a higher resolution for a grid map would have required too long computation time and an excessive amount of memory [7].

Fig. 7 depicts the South polar Integral illumination map for a mission epoch starting from 1 Jan. 2016, 11:00 h Universal Time Coordinate Gregorian (UTCG), to 1 Jan. 2017, 11:00 UTCG. The Earth vector represents the  $0^\circ$  meridian, which points upwards, in conformance to an agreed convention. In this direction and on the Earth-facing slope of the Malapert Mountain, an artefact can be

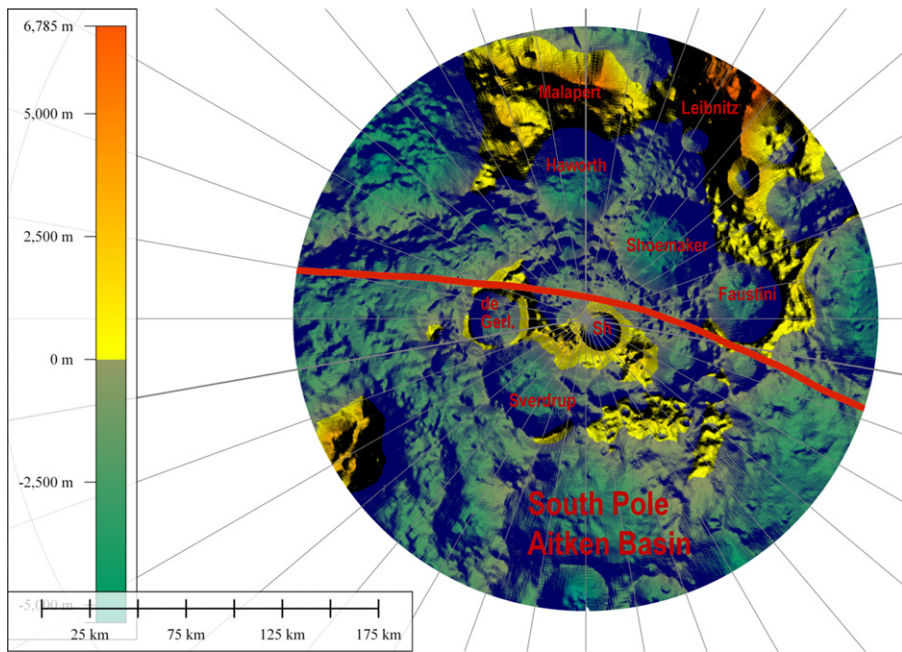


**Fig. 6.** Lunar South polar terrain relief from Kaguya Digital Elevation Model (altitude colour encoding, gnomonic polar projection).

detected, which is due to a defect within the Kaguya medium-resolution DEM, and which was also reported in [12].

As the Sun “moves”  $360^\circ$  azimuth along the horizon during one month the terrain is illuminated with a grazing incidence from all sides. Hills or mountain at the local horizon cast shadows on adjacent territory. The colour scale encodes the overall illumination time percentage of the grid points. The red spots indicate the peaks of near-eternal light. These are indicated with captions, as they have been considered for a detailed analysis of their appropriateness as landing locations (Section 2.3).

For the fixed height of the solar generator of 2 m it can be read from Fig. 7, that the farther away from the pole any landing location is, the higher this location has to be in order to gather a solar illumination with high percentage. A maximum integral illumination for the year 2016 of 293 days was detected for the Shackleton crater rim.

### 3.2. Integral annual ground contact percentage map

In order to establish a radio communications link for scientific data telemetry download or operations tele-command upload, a line-of-sight visibility towards the ground station is required. The amount and duration of ground contacts is a terrain characteristic that was analysed for the ESA Lunar Lander Mission and for a single deep-space ground antenna. The characteristics of the selected ESA Deep Space Antenna 1 (DSA 1) at New Norcia (Australia) are:

- Diameter: 35 m
- Coordinates:  $31.05^\circ$  South and  $116.20^\circ$  East

- Altitude: 252.26 m
- Min. elevation:  $5^\circ$  over the local horizon

The visibility of the ground station is characterised by daily visibility windows of approximately 11 h, which are contrasted by visibility gaps of approximately 13 h per day. In addition, monthly communication gaps of approximately 15 days occur. These gaps are qualitative and quantitative drivers for the operations concept and the On-Board Data Handling (OBDH) subsystem of the lunar lander craft, since they determine the degree of autonomy and the storage volume for scientific measurement and health status data.

The cumulative ground contact map in Fig. 8 features a colour scale that represents the ground station contact time in percentage of the year 2016. This analysis was also based on the Digital Elevation Model number 2, as described in Section 2.3, and the derived STK-model with a triangular mesh of 474 m granularity. The map reveals a high coverage for the nearside polar region close to the upper latitude of  $85^\circ$  South of the area of interest. This area is the Earth-facing slope of the Malapert Mountain. As it is located in almost direct line of sight between the South Pole and the Earth, it obstructs large areas of the South polar terrain from direct view to the ground antenna. The effect of shadowing of terrain by this mountain is illustrated by Fig. 5. It can also be seen that the polar region on the far-side, located within the South Pole Aitken basin, features comparatively poor ground contact durations.

### 3.3. Selection of candidate landing sites

Four quality criteria for the selection of candidates landing sites have been determined, which were

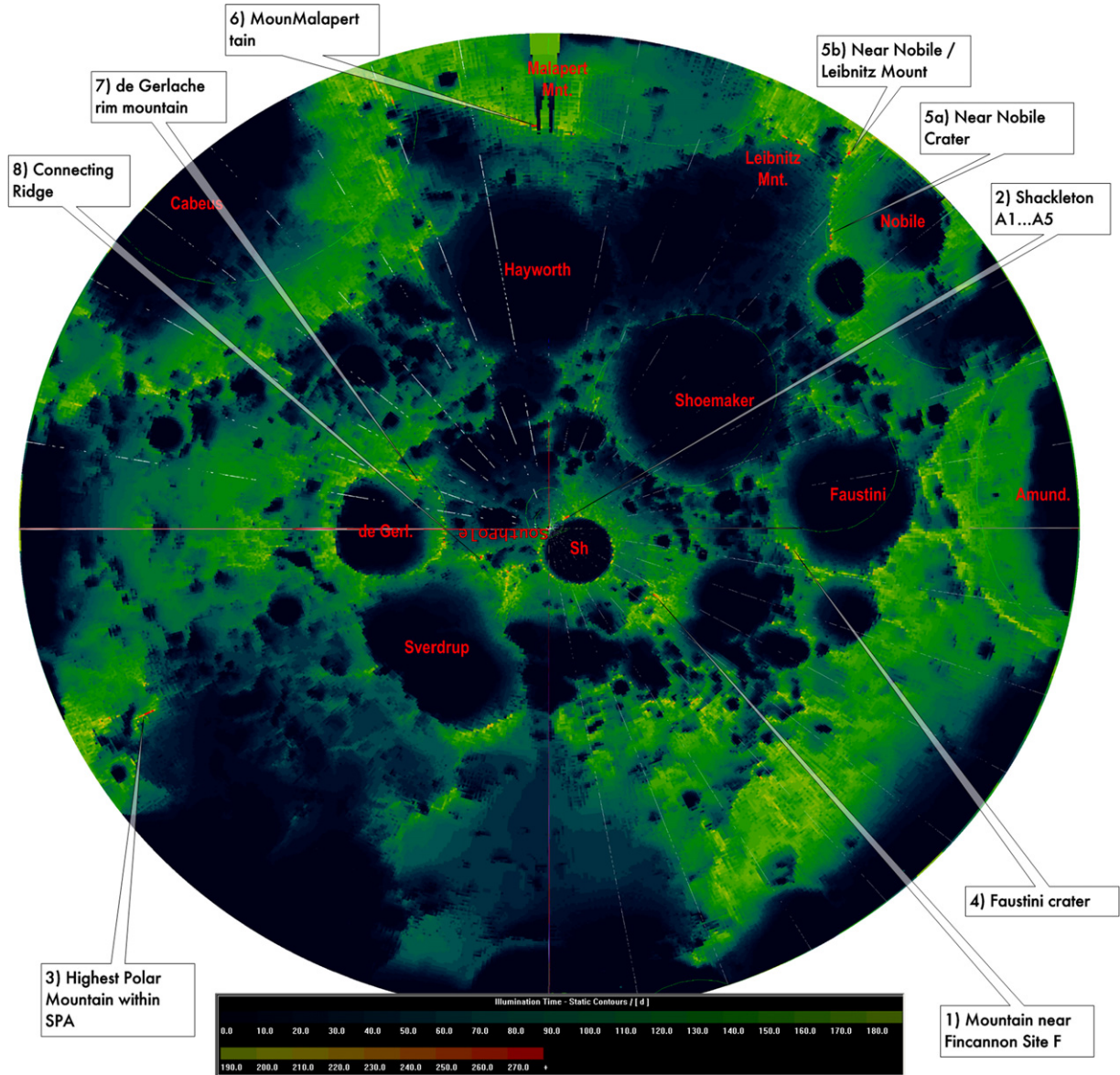


Fig. 7. Map of cumulative illuminated days at the lunar South Pole ( $-85^{\circ}$  ...  $-90^{\circ}$ S).

accounted for with different weighting factors. The first quality criterion is the overall illumination percentage. This is the most important criterion, therefore receiving a “KO-weighting” so that all but the best illuminated landing locations are excluded. Secondly, the temporal percentage of ground station contact is important for operations and telemetry resources demand. As the third criterion, the actual size of the area with favourable characteristics is driving the required landing accuracy. The larger the ellipse of touchdown dispersions along and across-track of the touchdown trajectory is allowed to be, the less demanding are the requirements on the accuracy of the lander craft’s subsystem for Guidance, Navigation and Control (GNC). As an additional quality criterion, the location of a landing site relative to the SPA Basin was

determined, but not considered in the ranking. Accredited lunar geologists want to deploy scientific payloads in the SPA Basin, as mentioned in Section 1.1, but their expert assessment of landing locations was not provided during the study [8].

Table 1 provides a list of the resulting integral illumination and ground contact percentages, together with the precise location of all landing sites indicated in Fig. 7.

### 3.4. Detailed illumination and ground contact timeline analyses

In practice, the integral illumination percentage of any landing location contains no detailed information on the amount and duration of shadow periods, so that the

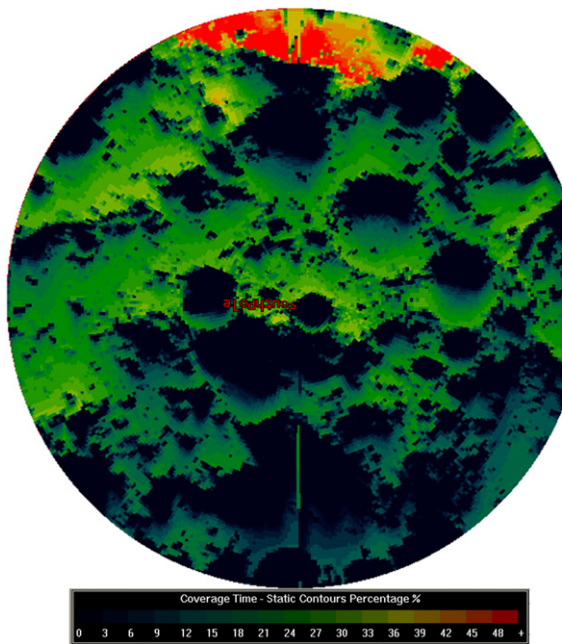


**Fig. 8.** Map of cumulative ground contact percentages with New Norcia DSA 1 during 2016.

problem of how to survive periods of darkness remains unsolved. The amount and duration of darkness periods for any landing site is low during the lunar summer season on the South Pole, and increases with the diminishing solar elevation angles of the approaching winter season. If a short mission takes place entirely during the local summer, the power subsystem of any lander or rover vehicle needs to bridge only short shadow periods. The desired overall mission duration therefore is a key parameter, which translates into a mission requirement that drives the power subsystem of any manned or robotic lander craft.

The effects of the lunar mission duration on the power subsystem sizing can be derived from the diagram of Fig. 9, which was generated by Fincannon with the help of a Digital Elevation Model and an analytical tool for the Shackleton landing site A1 [11]. For each of the 12 lunar days of the exemplary year 1994 the mean values of the illumination percentage are indicated in this graphic as a black line, the values of which can be read from the left hand side ordinate. With Fincannon's analysis method, the succession of shadowed and illuminated periods is simulated and the required worst case energy demand from the battery is calculated. The required amount of energy stored within the battery is indicated in dependence of the recharge ratio, which is the parameter of the coloured array of curves. The energy storage hours of the required battery can be read from the right hand side ordinate. The recharge ratio is calculated as the ratio of discharging power during periods of darkness versus the charging power during the illuminated periods. It indicates the relative performance of the lander craft's solar generator, which is the rapidity, with which the batteries can be fully recharged before the Sun again is obstructed by any

mountain at the horizon. Assuming that the operational power demand of a lunar station is equal in the illuminated and in the periods of darkness, a recharge ratio of unity would mean that the solar generator is approximately twice the size as required for mere operations, thus being able to recharge the battery in about the same duration as any preceding darkness period, not considering losses through non-ideal power electronics efficiency.

Generally the recharge ratio is driven by the available resources of the lander craft. Assuming that the size of the lander craft is restricted by the launcher capacity, the solar panel area and battery capacity are also limited. If a comparatively large payload suite is required to be operated during daylight, then only a small surplus power is available for battery recharging. Thus, the battery size remains small, and most payloads needed to be switched off during the shadowed periods. This was the case for the ESA Lunar Lander craft as designed during the study [8]. In addition, a conservative approach needed to be made for the power subsystem, because of the lack of a precise lunar Digital Elevation Model and associated reliable simulation tools, when the mission was conceived [8]. The mission duration was required to be one year, and the operational power demand during solar eclipses was reduced by a minimum dormant mode. Albeit a low recharge ratio of 0.05, the battery energy was required to bridge 200 h of darkness, which were assumed to be followed by 700 h of uninterrupted sunlight.

For the detailed illumination analysis, the South polar relief was modelled using the high-resolution Kaguya Digital Elevation Model, described in Section 2.3 and denoted as DEM number 3. The grid granularity of the STK model was compatible with the DEM resolution of 1/128° in latitude of the terrain, which was equal to 237 m. As an STK analysis output, an ASCII report containing the evolution of illumination for each region and for each single grid point of the model has been exported. All 11 candidate landing sites from Table 1 within the 8 regions as indicated in Fig. 7 were analysed in this way, and for the most promising two sites the detailed results are presented in the following.

Fig. 10 depicts the integral illumination time for a detailed DEM of the Shackleton crater rim during the year 2016. Depicted is also the ring topology of the analysis terrain, which was reduced in order to save processing time.

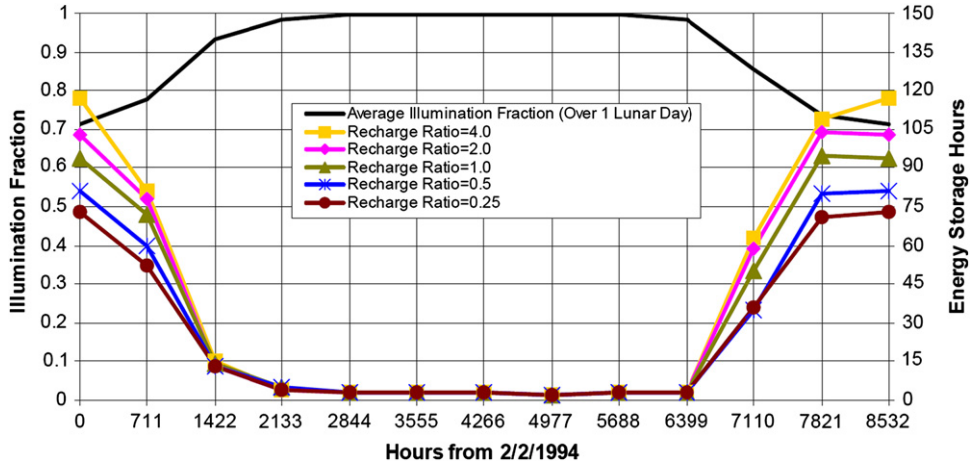
Fig. 11 depicts the integral illumination time for the detailed DEM of the Connecting Ridge between Shackleton and de Gerlache Craters during the year 2016.

For the two exemplary sites of Figs. 10 and 11 and during the mission epoch of 5 years (2016–2020), the annual evolutions of the illumination and ground contact conditions were post-processed by a calculation spread sheet. A moving weekly average of illumination hours was plotted for each of the five years. Added to this, the daily ground contact hours were plotted in the same diagram. The results of these analyses are depicted in Fig. 12 for the Shackleton crater rim (sites 2a to 2e in Table 1) and in Fig. 13 for the Connecting Ridge between Shackleton and de Gerlache craters (site 8 in Table 1). These chronological sequences are crucial for the design and operations of any future lander craft.

**Table 1**

Suggested landing sites for detailed illumination analysis.

| No. | Site name acc. OHB analysis             | Latitude | Longitude | Illumination per 2016[%] | G/S visibility per 2016[%] |
|-----|---|----------|-----------|--------------------------|----------------------------|
| 1   | Mountain near Fincannon site F          | 88°48'S  | 124°17'E  | 71.7                     | 33                         |
| 2a  | Shackleton A1                           | 89°24'S  | 161°24'E  | <b>80.4</b>              | 28                         |
| 2b  | Shackleton A2                           | 89°47'S  | 153°24'E  | 67.6                     | 27                         |
| 2c  | Shackleton A3                           | 89°54'S  | 143°12'E  | 66.5                     | 27                         |
| 2d  | Shackleton A4                           | 89°47'S  | 54°50'E   | 71.6                     | 30                         |
| 2e  | Shackleton A5                           | 89°18'S  | 124°36'W  | 68.4                     | 28                         |
| 3   | Highest Polar Mountain within SPA       | 85°08'S  | 117°16'W  | 76.7                     | 33                         |
| 4   | Faustini Crater towards pole            | 87°43'S  | 95°32'E   | 67.4                     | 30                         |
| 5a  | Near Nobile Crater                      | 86°7'S   | 43°30'E   | 68.3                     | 25                         |
| 5b  | Near Nobile/Leibnitz Mountain           | 85°17'S  | 37°9'E    | 78.4                     | 41                         |
| 6   | Malapert Mountain                       | 85°59'S  | 2°15'W    | 79.9                     | <b>47</b>                  |
| 7   | de Gerlache rim mountain                | 88°39'S  | 68°31'W   | 68.3                     | 30                         |
| 8   | Connecting Ridge Shackleton/de Gerlache | 89°25'S  | 137°06'W  | 73.0                     | 36                         |
| 9   | Montain 1 within SPA                    | 87°16'S  | 127°31'E  | 60.5                     | 30                         |
| 10  | de Gerlache outer rim                   | 87°59'S  | 95°30'W   | 62.0                     | 30                         |
| 11  | Malapert near Haworth crater            | 86°59'S  | 24°21'W   | 64.8                     | 27                         |

**Fig. 9.** (Colour online) Annual effect of solar elevation on Shackleton site A1 illumination fraction and energy storage hours (reprinted from [11]).

Both in Fig. 12 and in Fig. 13 it is possible to notice the drift of South Pole Summer (highest continuous average illumination) and winter (lowest continuous average illumination) during the epoch years. Although the integral illumination of both sites is comparable, it can be seen from the weekly moving illumination averages that both frequency and duration of solar eclipses are distinctly different. From these results it is obvious that a detailed analysis of the succession of illuminated and shadowed periods is necessary to provide details of the photovoltaic power influx. The gap analysis described in the following Section 3.5 is a prerequisite for correctly designing a lander craft's power subsystem.

### 3.5. Illumination gaps analysis

In order to quantify the requirements for the power subsystem of any lunar lander craft or base, the South polar illumination results were further analysed for the precise occurrence and lengths of shadow periods. For this purpose a MatLab analysis script was programmed

that read and processed the illumination timelines. Following is a description of exemplary results for the Shackleton crater rim (sites 2a to 2e in Table 1) and for the Connecting Ridge between Shackleton and de Gerlache craters (site 8 in Table 1).

The Fig. 14 depicts the longest continuous illumination map at the Shackleton Crater Rim, which is the maximum uninterrupted sunlit period that can be found during the local summer season. It can be read that for the Shackleton site A2 this duration is approximately 3515 h, followed by sites A4 and A1.

Also for the Shackleton crater rim, Fig. 15 depicts the longest illumination map with allowed intermittent interruptions, which are specified as shadow periods not exceeding 10 h. It can be read that for the Shackleton site A2 this duration also amounts to 3515 h. From this identity it can be deduced that the shortest shadowed period at Shackleton crater rim is longer than 10 h.

If dark periods of 24 h are allowed, Fig. 16 reveals that landing places at the Shackleton crater rim can be found with quasi-continuous illumination of approximately 4183 h.

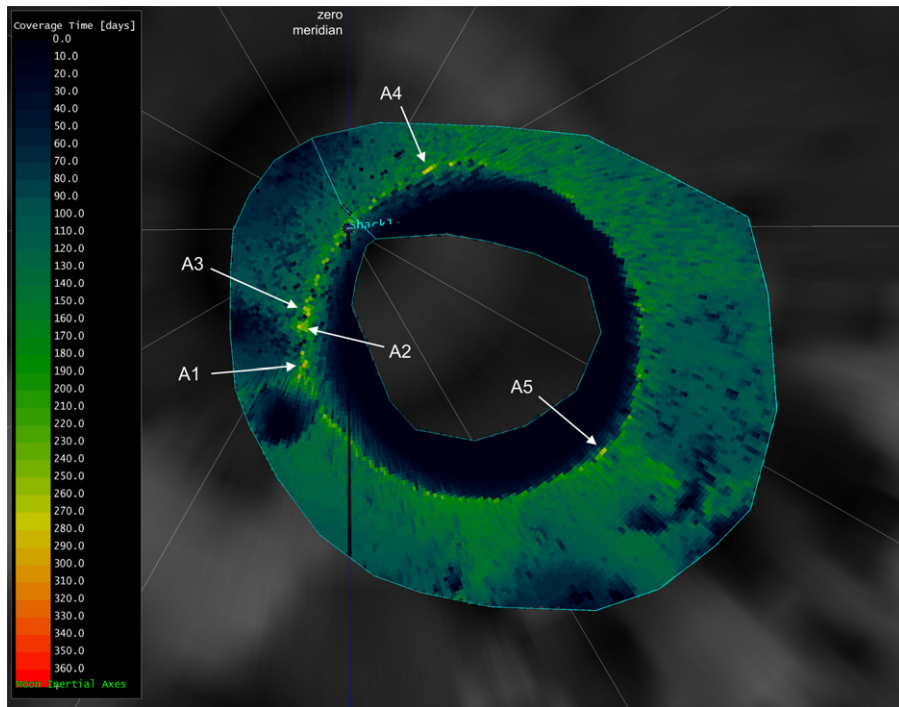


**Fig. 10.** Detailed illumination results at the Shackleton Crater Rim.

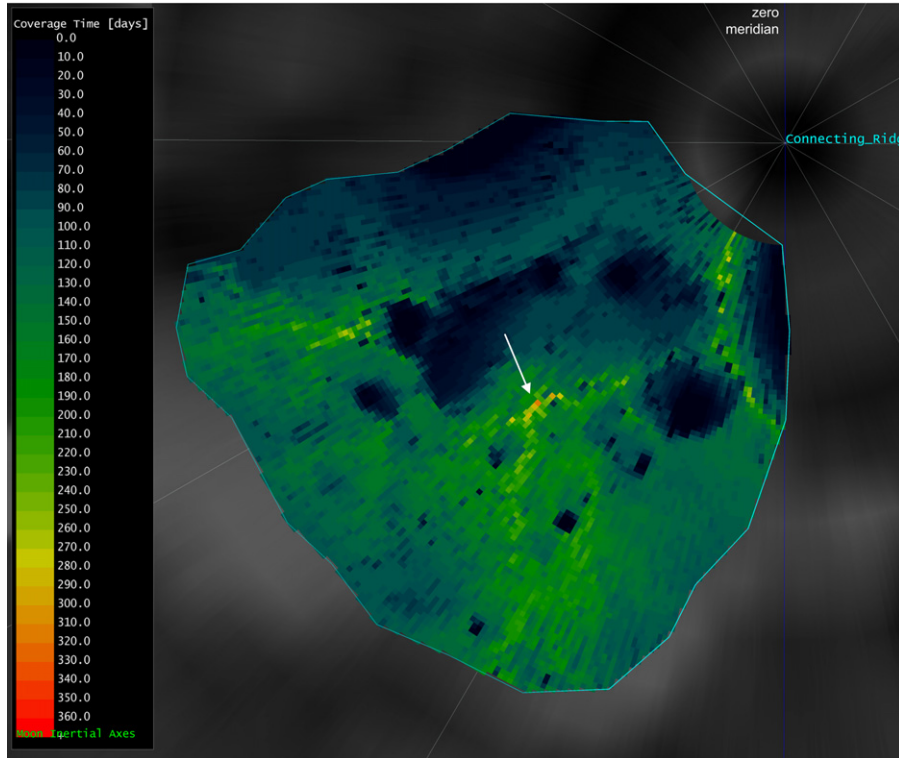


**Fig. 11.** Detailed illumination results at the Shackleton-de Gerlache Connecting Ridge.

Finally, Fig. 17 depicts the longest illumination map with allowed intermittent interruptions of 120 h. It can be

read that for the Shackleton site A2 this duration is approximately 7740 h. With enough battery energy

resources to sustain 120 h of darkness, the overall mission duration at these places can be extended up to almost one year, that is approximately 322 days.

The Fig. 18 depicts the longest continuous illumination map at the Connecting Ridge between Shackleton and de

Gerlache Craters, of which the maximum duration can be read as approximately 5588 h.

Also for the Connecting Ridge between Shackleton and de Gerlache Craters, Fig. 19 depicts the longest illumination map with allowed intermittent interruptions, which

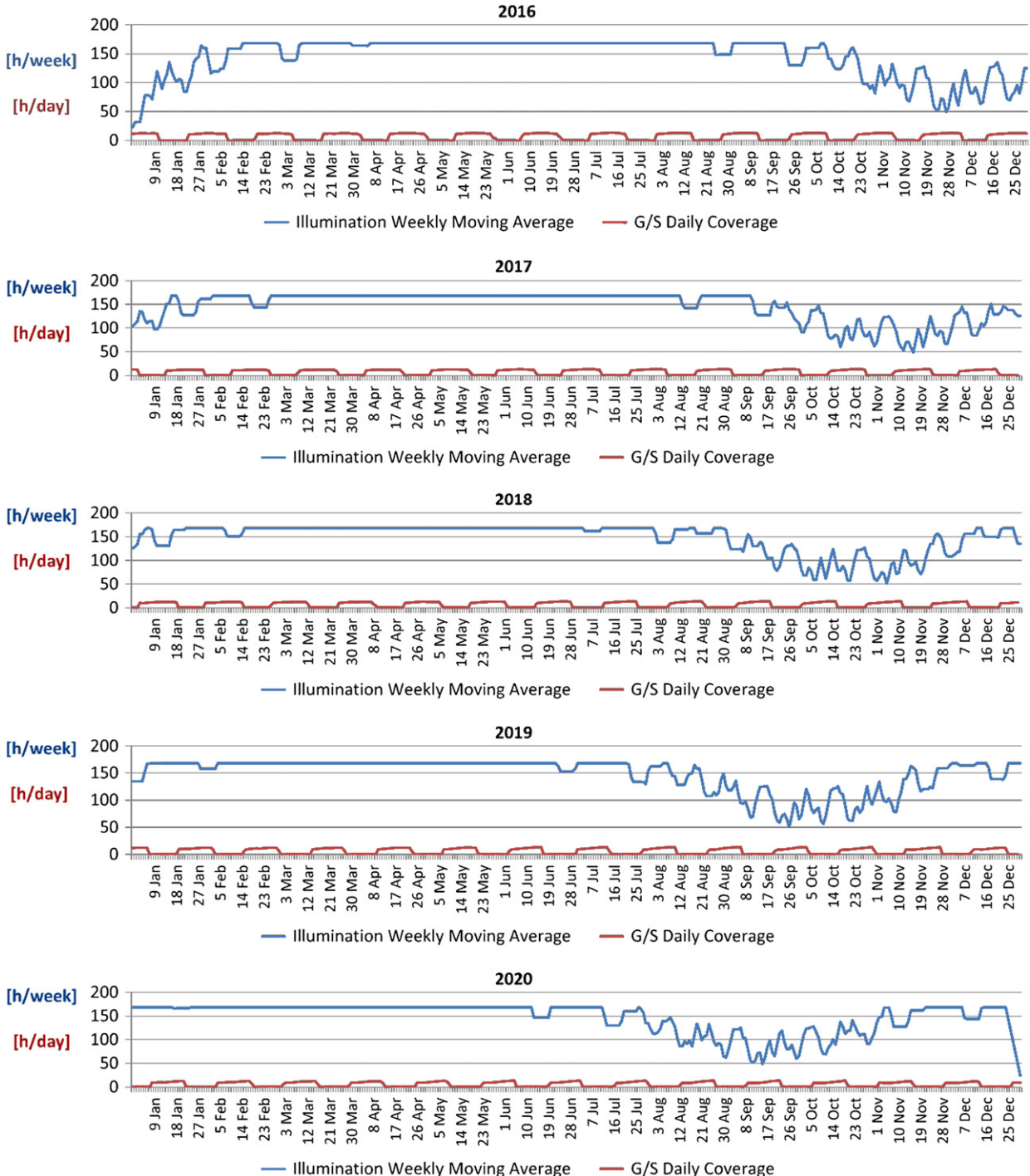
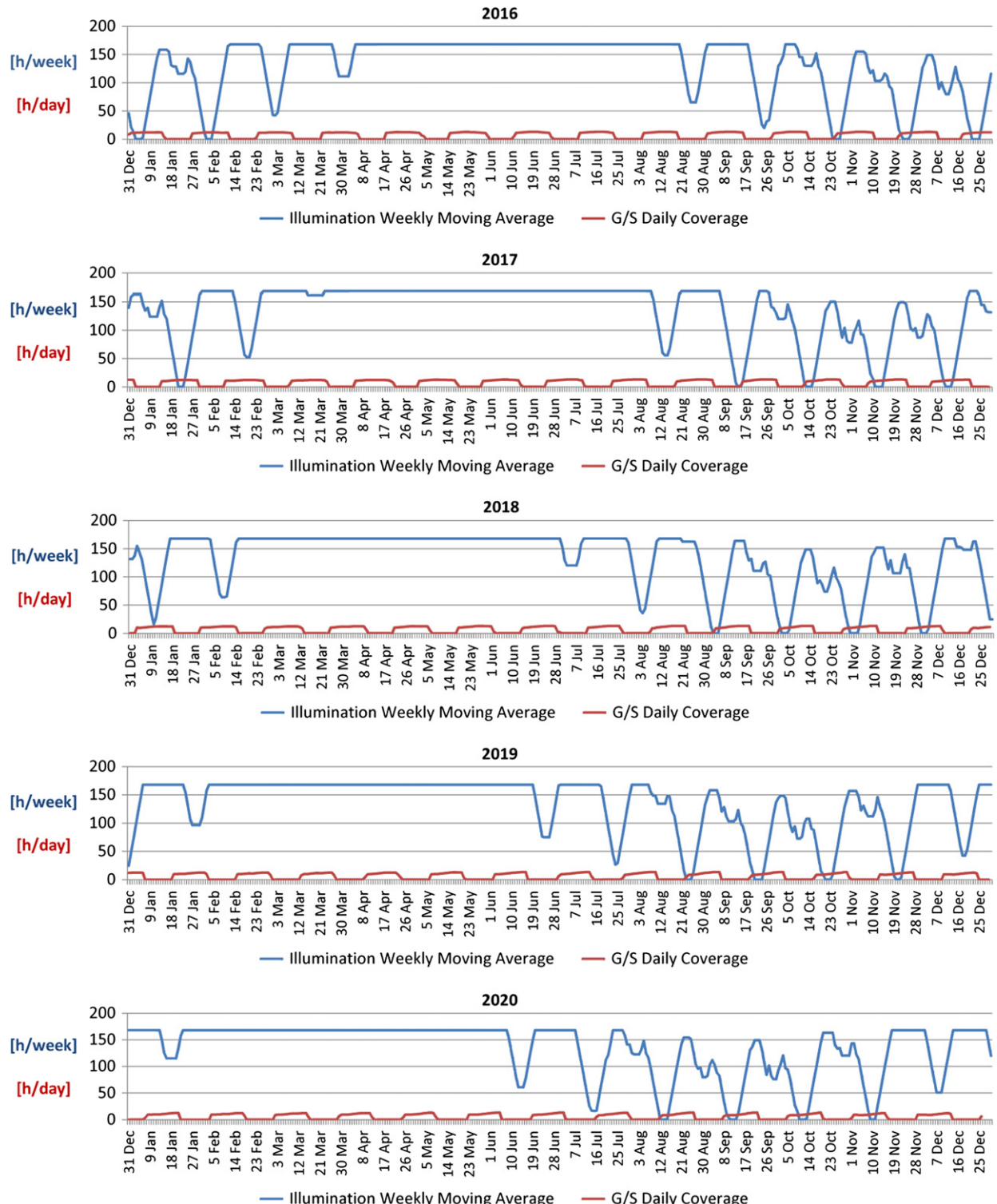


Fig. 12. (Colour online) Moving weekly and daily averages of illumination and ground contacts for Shackleton A2 through the mission epoch.

are specified as shadow periods not exceeding 10 h. It can be read that for the Connecting Ridge between Shackleton and de Gerlache Craters this duration also amounts to

5588 h. From this identity it also can be deduced that any shadowed period at this landing site is longer than 10 h.



**Fig. 13.** (Colour online) Moving weekly and daily averages of illumination and ground contacts for the Shackleton–de Gerlache Connecting Ridge through the mission epoch.

If dark periods of 24 h are allowed, Fig. 20 reveals that landing places at the Connecting Ridge between Shackleton and de Gerlache Craters can be found with quasi-continuous illumination of approximately 5954 h.

Finally, Fig. 21 depicts the longest illumination map with allowed intermittent interruptions of 120 h. It can be read that for the Connecting Ridge between Shackleton and de Gerlache Craters this duration is approximately 6840 h. With enough battery energy resources to sustain 120 h of darkness, the overall mission duration at this landing site can be extended up to approximately 285 days.

Table 2 represents the summary of simulation results for the longest continuous illumination periods with predefined gaps for all 8 landing areas. The maximum values are highlighted through bold letters.

The values of the provided longest quasi-continuous illumination periods have been determined in an interactive

process from the illumination maps provided by the MatLab environment.

It is remarkable that the landing area no. 8, which is the Connecting Ridge between the Craters Shackleton and de Gerlache, features by far the longest quasi-continuous illumination periods with allowed gaps of 10 and 24 h, and ranks among the longest illumination periods with gaps of 120 h.

Furthermore, it can be read from Table 2 that the measured landing site extensions are highest for the terrain elevations with the largest curvature. This is especially given for the large mountain summits within the South polar region, with a maximum value for Highest Polar Mountain within the SPA, which is indicated as number 3 in Table 2. This finding reflects the theoretical considerations of Section 2.1 respectively [10].

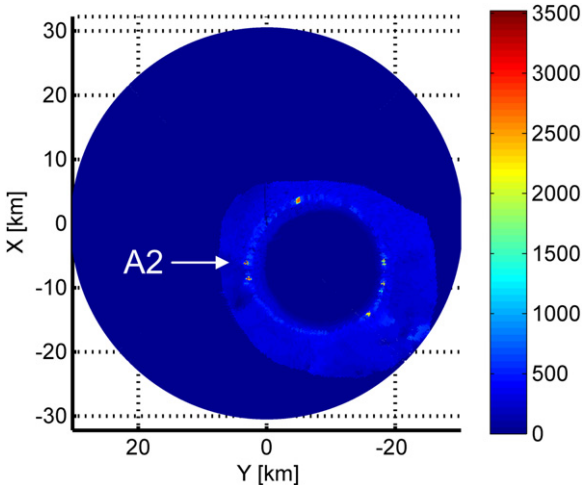


**Fig. 14.** Map indicating the longest uninterrupted illumination at the Shackleton crater.

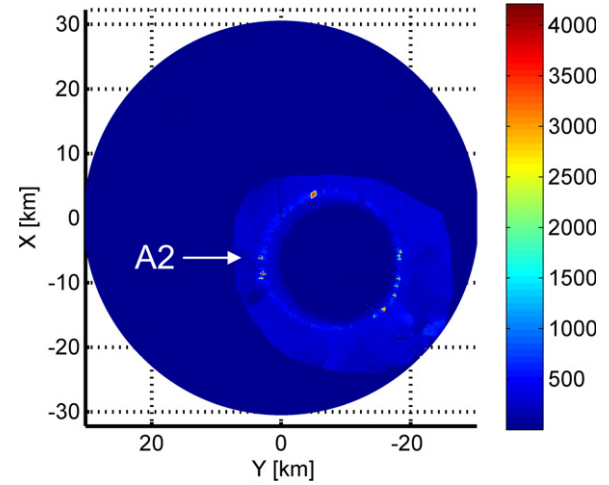


**Fig. 16.** Quasi-continuous illumination map including shadows of 24 h at the Shackleton crater.

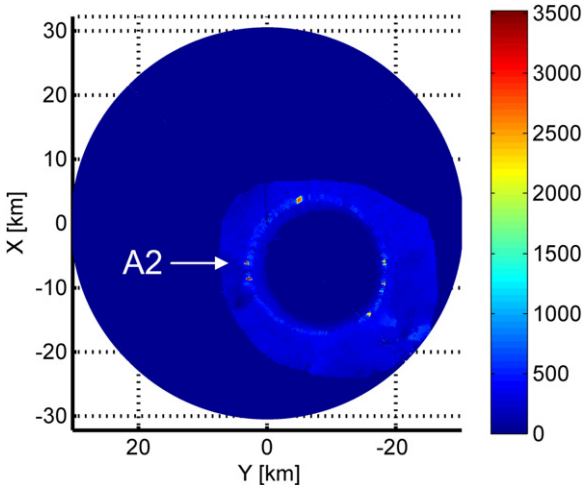


**Fig. 15.** Quasi-continuous illumination map including shadows of 10 h at the Shackleton crater.

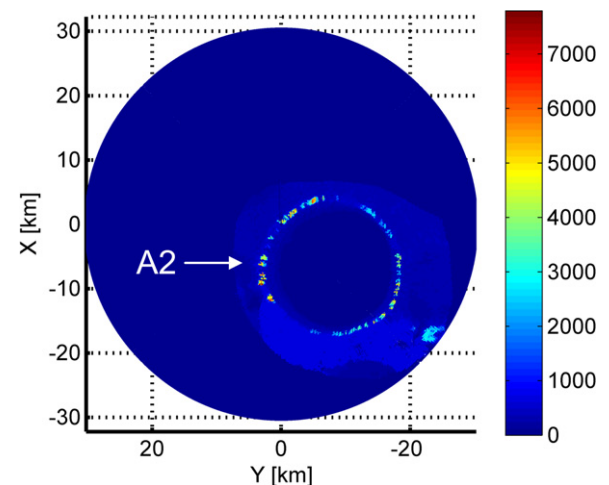


**Fig. 17.** Quasi-continuous illumination map including shadows of 120 h at the Shackleton crater.

## 4. Verification and error analysis

### 4.1. Comparison of simulation and remote sensing imagery

For a verification of the analysis tool chain consisting of the DEM import process and the illumination simulation a pragmatic approach through similarity considerations was performed. The Fig. 22 depicts a comparison between STK illumination results and 4 Kaguya High Definition Video stills from the video film number V-044-0158 [26]. The video was generated on December 11, 2008, with the camera pointing nadir, which means in local vertical direction. The first image on the left hand side of Fig. 22 was exposed at 14:08:06 UTCG. The area of interest is the Lunar South Pole, which is the Shackleton crater area and its vicinity. The illumination map was simulated with the STK software suite for the same mission epoch and with our model number 2, as described in Section 2.3. The result is shown on the right hand side of

Fig. 22 as a yellow pattern for the illuminated area, which is superimposed onto the ground relief. The comparison reveals good coincidence of the illuminated areas over the whole area of interest. As under these low sun incidence angles even small errors in the implementation of the ephemerides, DEM or illumination calculation, would have large impact on the illuminated areas, it has been concluded that no systematic errors have been made in the simulation set-up and therefore also the detailed analysis of the potential landing sites is only limited by the DEM quality.

### 4.2. Comparison of analysis results

The comparison of the quantitative results of Table 2 with those of other teams is difficult, because the selected locations differ slightly. From the five selected locations by Bussey et al. [14] only one has the exact same coordinates. This is the de Gerlache rim mountain, which is indicated as number 7 in Table 2, and as letter D in [14]. The integral or

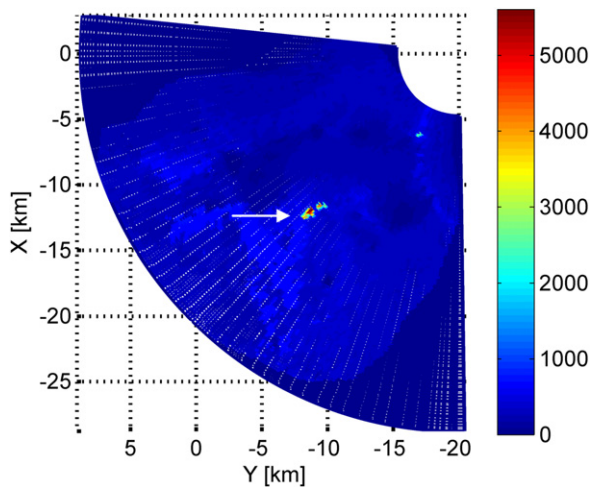


**Fig. 18.** Map of longest uninterrupted illumination at the Shackleton-de Gerlache Connecting Ridge.

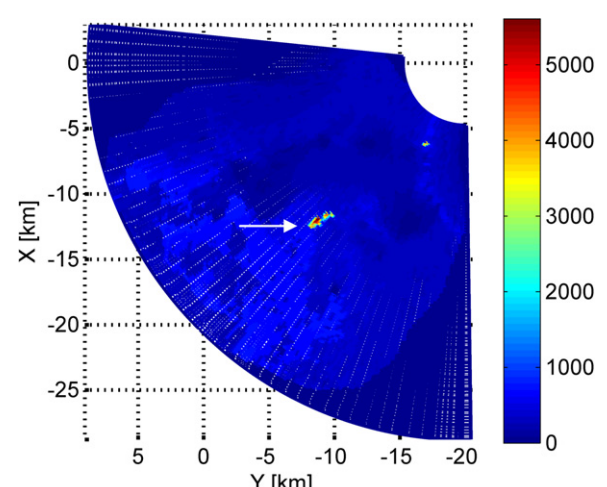


**Fig. 20.** Quasi-continuous illumination map including shadows of 24 h at the Shackleton-de Gerlache Connecting Ridge.

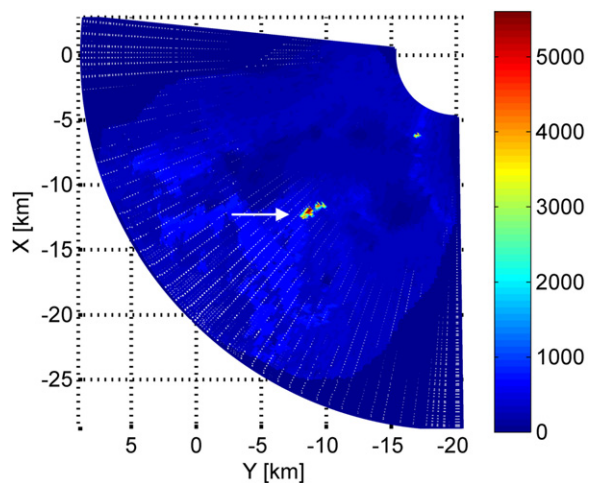


**Fig. 19.** Quasi-continuous illumination map including shadows of 10 h at the Shackleton-de Gerlache Connecting Ridge.

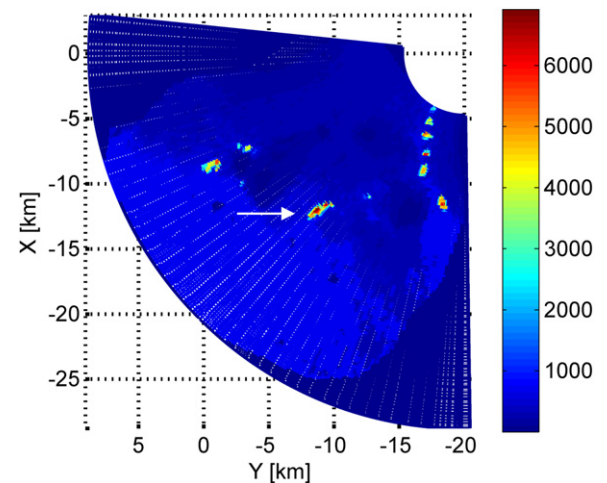


**Fig. 21.** Quasi-continuous illumination map including shadows of 120 h at the Shackleton-de Gerlache Connecting Ridge.

**Table 2**

Summary of analyses results for longest continuous illumination periods with predefined gaps.

| No/ [ ] | Site name                               | Lat./ [°] | (Hemisphere) | Long./ [°] | (Hemisphere) | Altitude/ [km] | Integral illum. time per year/[%] | Site extension/ [km <sup>2</sup> ] | Illum. period w/o shadows/ [h] | Illum. period incl. 10 h shadows/[h] | Illum. period incl. 24 h shadows/[h] | Illum. period incl. 120 h shadows/[h] |
|---------|---|-----------|--------------|------------|--------------|----------------|-----------------------------------|------------------------------------|--------------------------------|--------------------------------------|--------------------------------------|---------------------------------------|
| 1a      | Mountain near Fincannon site F#1        | 88°49' S  |              | 123°54' E  |              | 1630           | 74.55                             | 0.080                              | 1174                           | 1137                                 | 2472                                 | 4855                                  |
| 1b      | Mountain near Fincannon site F#2        | 88°52' S  |              | 132°29' E  |              | 1421           | 75.97                             | 0.666                              | 4183                           | 4220                                 | 4642                                 | 5481                                  |
| 2a      | Shackleton A4                           | 89°47' S  |              | 54° E      |              | 1420           | 78.76                             | 0.168                              | 2869                           | 2947                                 | 3816                                 | 6388                                  |
| 2b      | Shackleton A1                           | 89°42' S  |              | 161°55' W  |              | 1681           | 83.26                             | 0.058                              | 2680                           | 2855                                 | 3449                                 | 6864                                  |
| 2c      | Shackleton A2                           | 89°46' S  |              | 153°18' W  |              | 1713           | 78.68                             | 0.058                              | 3515                           | 3515                                 | 4183                                 | <b>7740</b>                           |
| 2d      | Shackleton A3                           | 89°48' S  |              | 154°47' W  |              | 1660           | 73.52                             | 0.168                              | 1324                           | 1320                                 | 1444                                 | 4213                                  |
| 2e      | Shackleton A5                           | 89°18' S  |              | 131°07' E  |              | 1276           | 71.10                             | 0.125                              | 2301                           | 2333                                 | 2889                                 | 5369                                  |
| 3       | Highest Polar Mountain within SPA       | 85°42' S  |              | 116°32' W  |              | 2873           | 79.21                             | <b>1.037</b>                       | 1395                           | 1393                                 | 2061                                 | 4786                                  |
| 4       | Faustini Crater                         | 87°46' S  |              | 95°01' E   |              | 0562           | 67.52                             | 0.849                              | 575                            | 632                                  | 632                                  | 4748                                  |
| 5a      | Near Nobile Crater#1                    | 85°18' S  |              | 37°09' E   |              | <b>6748</b>    | 78.67                             | 0.055                              | 4584                           | 4585                                 | 5294                                 | 7198                                  |
| 5b      | Near Nobile Crater#2                    | 85°34' S  |              | 37°38' E   |              | 6027           | 76.10                             | 0.324                              | 3771                           | 3906                                 | 3725                                 | 5415                                  |
| 5c      | Near Nobile–Leibniz Mountain            | 85°28' S  |              | 31°06' E   |              | 6290           | 73.54                             | 0.529                              | 4712                           | 4757                                 | 4951                                 | 4672                                  |
| 6a      | Malapert Mountain#1                     | 85°58' S  |              | 3°6' W     |              | 4931           | 77.39                             | 0.203                              | 2692                           | 2833                                 | 3085                                 | 6356                                  |
| 6b      | Malapert Mountain#2                     | 86° S     |              | 2°10' E    |              | 5137           | 73.73                             | 0.608                              | 4224                           | 4708                                 | 4885                                 | 6647                                  |
| 7       | de Gerlache Rim Mountain                | 88°41' S  |              | 68°20' W   |              | 1750           | 80.54                             | 0.123                              | 3835                           | 4222                                 | 4222                                 | 6901                                  |
| 8       | Connecting Ridge Shackleton/de Gerlache | 89°28' S  |              | 136°40' W  |              | 1947           | <b>85.71</b>                      | 0.125                              | <b>5588</b>                    | <b>5588</b>                          | <b>5954</b>                          | 6840                                  |

mean illumination percentages are calculated to 80.54% in Table 2 versus >80% in [14]. The Malapert Mountain rim locations M1 and M2 of [14] are calculated to collectively feature 74% of illumination, and in Table 2 the Malapert Mountain site number 6, which seems to coincide with M2 is calculated as 73.73%. The prominent Shackleton crater rim location A in [14] does not exactly match the coordinates of site A1 in Table 2, but the illumination results do match with >80% in [14] versus 83.26% in Table 2. It can thus be concluded that there is a very good coincidence between the present analysis results and those of [14].

Another verification approach was performed by comparing the present illumination results of Table 2 with a similar map, depicted in Fig. 23, that was generated by a ray-tracing algorithm and a DEM derived from Kaguya data [12]. McCloskey uses a DEM with a resolution of 500 m granularity, and a linear interpolation for missing altitude grid values within the terrain below  $-85^{\circ}$  latitude. The mission epoch is the year 2008. The applied illumination method is a Sun–Moon single illumination vector interpolation. It was found that at the outer rim of the polar area, the qualitative appearance of the shadowed regions in Fig. 23 is different from the one presented, meaning that there seem to be some shadows missing in the map of Fig. 23. In [12] the existence of gouges in the generated DEM above  $-85^{\circ}$  latitude is stated, which are accounted to the described edge mismatch. Apart from these deviations, both maps are in qualitative good accordance. The maximum illumination values read from Fig. 23 are approximately 90% versus 85.71% of Table 2. This may be attributed to a different height of the ground assets definition, of which there are no details specified in [12].

Finally, a comparison with a NASA illumination analysis based on Lunar Reconnaissance Orbiter (LRO) altimetry data was performed. The NASA illumination map was generated by Mazarico et al. [15] using a Lunar DEM originating from the Lunar Orbiter Laser Altimeter dataset. The map of Fig. 24 shows the average illumination of the South Pole region over four lunar precession cycles in per cent. Permanent shadowed regions appear in black. Locations with highest average illumination are highlighted in pink, distributed in a few clusters. A best-illuminated point was found near the Shackleton crater, which features average Sun visibility of 92.7% at surface level. The comparison shows a qualitative match with the present analysis results, but a mismatch of the absolute illumination percentages. The reasons for this are assumed to be twofold, namely

- An increased fineness of the LRO DEM compared to that of Kaguya,
- a different assumed height of the illuminated lander craft. In Mazarico et al. [15] heights of 0 m and 10 m above the terrain have been analysed, while in the present analysis a height of 2 m has been assumed.

#### 4.3. Error estimation

An error analysis for the results of the present calculations is a complex task, as described in the following. Along the processing chain from the Laser instrument to

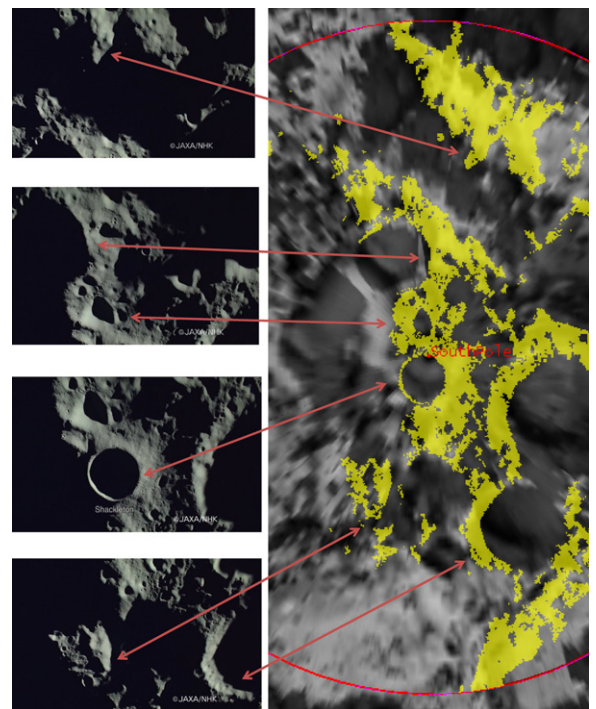
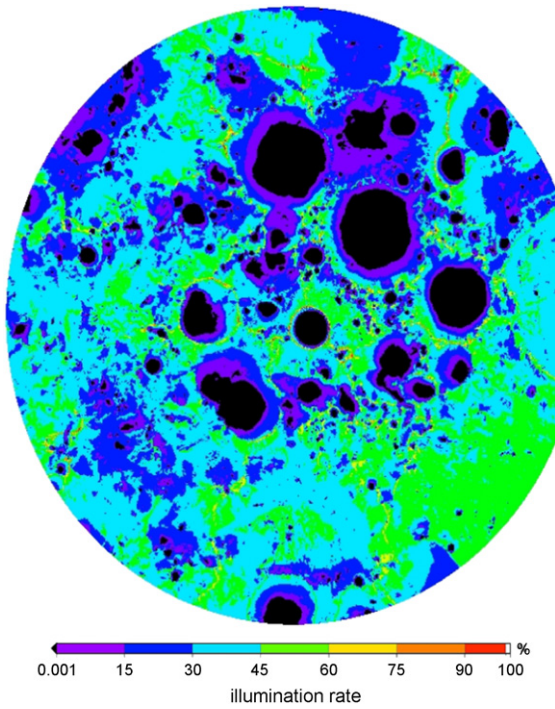


Fig. 22. Kaguya HDTV stills versus STK illumination pattern on lunar DEM (areas with direct sun illumination are shown in yellow colour).

the illumination timeline for each grid point onto the lunar DEM, the following error contributions must be considered.

- The uncertainty with which the position of a feature on the lunar surface can be predicted in inertial space is generally denoted as map-tie error. Since altitude sounding values from orbit are used to locate features of the digital elevation model in inertial space, the associated accuracy depends on instrument pointing, orbit determination, and other errors associated with the measurements taken from orbit.
- The result of the ray-tracing algorithm for the calculation of light or shadow for each grid point and during each time step has a limited accuracy, because not only the grid point and the light source, but also the obstructions have limited position accuracies.

In order to estimate the typical error associated to the illumination analyses, the following exemplary scenario is examined. The lunar lander craft or base may be located at the rim of the Shackleton crater and the Sun be obstructed by the Malapert Mountain. The mean temporal error of solar emergence is calculated from the height error of the analysis model. In the Kaguya Laser Altimeter Product Format Description [23] the range precision of the topographic DEM (LALT\_GT\_SP\_NUM) is specified with an inherent standard deviation of  $\Delta h(\sigma)=5$  m. The Malapert Mountain flank inclination  $\gamma$  was read from a



**Fig. 23.** Lunar South Pole integral illumination map based on Kaguya/Selene DEM (reprinted from [12]).

projected image similar to that of Fig. 5 to amount to approximately  $19^\circ$ . The mean horizontal model error of the Malapert Mountain flank  $\Delta l(\sigma)$  is thus calculated as

$$\Delta l(\sigma) = \frac{\Delta h(\sigma)}{\tan \gamma} = 14.52 \text{ m}$$

The distance  $D$  between the Malapert Mountain and the Shackleton crater was determined to 122.07 km. With these values the uncertainty of the solar emergence angle  $\varepsilon(\sigma)$  is calculated as

$$\varepsilon = 2 \arcsin \frac{\Delta l(\sigma)}{2D} = 24.535''$$

For the further calculation the angular solar “motion”  $\dot{\lambda}$  is calculated as

$$\dot{\lambda} = \frac{(360^\circ/\text{month}) \times (3600''/^\circ)}{(31,558,150\text{s}/\text{year})/(12\text{months}/\text{year})} = 0.493''/\text{s}$$

The temporal uncertainty of the solar emergence  $\Delta\tau(\sigma)$  is thus calculated as

$$\Delta\tau(\sigma) = \frac{\Delta\varepsilon(\sigma)}{\dot{\lambda}} = 49.786\text{s}$$

With a 95.45% confidence interval of  $\pm 2\sigma$  the prediction certainty of the solar emergence time is calculated as  $\Delta\tau(\pm 2\sigma) = 3\text{ min}19\text{s}$

This estimation value is two to three orders of magnitude smaller than the considered illumination gaps that are relevant for the survival of the power subsystem of the lunar lander craft or base.

For the integral illumination analysis the uncertainties of the numerous solar dusk-dawn changes need to be

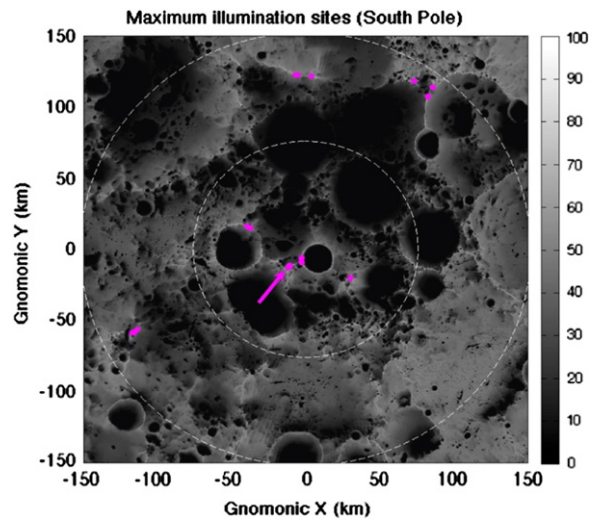


**Fig. 24.** (Colour online) Lunar South Pole Integral Illumination Map based on LRO DEM (reprinted from [15]).

added as the root of the squares sum. With an estimation of a mean value of 30 dusk-dawn transfers during a lunar day the calculated overall uncertainty of the integral illumination during one mission year  $\Delta T$  calculated as

$$\Delta T(\pm 2\sigma) = \sqrt{12 \times 30 \times \Delta\tau_i^2(\pm 2\sigma)} = 62 \text{ min}58\text{s}$$

This estimation value is several orders of magnitude smaller than the annual time for photovoltaic power generation.

## 5. Conclusions

The precise analyses of illumination and ground access conditions for an extended lunar terrain are a demanding task with respect to software algorithms and computing performance. Added difficulty emanates from the necessity of pre-processing of the digital elevation data, which is required in order to convert to Planetary Data System (PDS) compatible data formats. The post-processing of the timelines of illuminations for each point of the landing area assets grid overlaying the DEM in practice is also difficult for a number of reasons. For instance, there are no spherical co-ordinates available in MatLab so that mappings must be re-projected, which is not trivial.

In the present analyses, the integral illumination results from Noda et al. [13], McClanaghan [12], and Bussey et al. [14] were not only reproduced, but complemented by high-resolution maps. These were in line with later results from Mazarico et al. [15].

An illumination gap analysis was reported, the detailed results of which were listed for candidate landing sites as quasi-continuous illumination durations. For these sites the survival of a lander craft with battery energy for 10, 24, and 120 h was proven for the calculated quasi-continuous illumination durations. This work is complementing and extending similar analyses by Vanoutryve et al. [9]. An error estimation showed the applicability of the results.

The actual recommendation of landing sites is driven by the following criteria:

- The resources that the power subsystem of a lander needs to provide for darkness periods.
- The spatial extension of the landing area featuring favourable illumination conditions.
- The ground station visibility conditions.

In this respect, the Shackleton-de Gerlache Connecting Ridge terrain, denominated as Site no. 8 in all listings, provides the most favourable landing site quality.

The presented results should be confirmed by a new illumination gap analysis based on the even more precise DEM originating from the LRO altimeter instrument.

## References

- [1] James D. Burke, Merits of a lunar polar base location, JPL California Institute of Technology, The Planetary Institute, 1985.
- [2] Paul D. Spudis, The lunar environment: asset or liability? Conference on Astrophysics Enabled by the Return to the Moon, Space Telescope Science Institute, Baltimore MD, 28–30 November, 2006.
- [3] Marcus G. Langseth, Stephen J. Keihm, Kenneth Peters, Revised lunar heat-flow values. Proceedings of the 7th Lunar Scientific Conference, 1976. Lunar and Planetary Institute. Provided by the NASA Astrophysics Data System, 1976, pp. 3143–3171.
- [4] J.R. Arnold, Ice at the lunar poles, *J. Geophys. Res.* 84 (1979) 5659–5668.
- [5] Mark A. Wieczorek et al., The constitution and structure of the lunar interior, in: *Reviews in Mineralogy and Geochemistry*, vol. 60, 2006, pp. 221–364.
- [6] Sho Sasaki, the KAGUYA Gravity/Topography Team, The first precise global gravity and topography of the Moon by KAGUYA (SELENE) mission. Presentation B10-0014-10, Proceedings of the COSPAR, Bremen, 2010.
- [7] Chandra Wickramasinghe, Max K. Wallis, Carl H. Gibson, Jamie Wallis, Shirwan Al-Mufti, Nori Miyake, Bacterial morphologies in carbonaceous meteorites and comet dust. ArXiv at Cornell University Library, Ithaca (New York), 2010.
- [8] Maren Homeister, Joachim Thaeter, David Koebel, Jeffrey W.G.P. Apeldoorn, Capabilities of a lunar lander based on ariane-V shared launch opportunity. Proceedings of the 61st International Astronautical Congress, Prague, September 27 to October 1, 2010.
- [9] B. Vanoutryve, D. De Rosa, R. Fisackerly, B. Houdou, J. Carpenter, C. Philippe, A. Pradier, A. Jojaghaian, S. Espinasse, B. Gardini, An analysis of illumination and communication conditions near lunar south pole based on kaguya data. [Publication of the] European Space Agency, Directorate of Human Space Flight, Keplerlaan 1-2200 AG Noordwijk—The Netherlands.
- [10] Michiel Kruijff, The peaks of eternal light on the lunar south pole—how they were found and what they look like, SP-462, 4th Int. Conf. on Exploration and Utilisation of the Moon (ICEUM4). ESA/ESTEC, September 2000.
- [11] James Fincannon, Lunar south pole illumination: Review, Reassessment, and Power System Implications. (NASA Glenn Research Center). AIAA 2007-4700. AIAA 5th Int. Energy Conv. Eng. Conference (IECEC), St. Louis, Missouri, 2007.
- [12] Tim P. McClanahan, North and South Pole (80–90°) Targets from Kaguya LALT (Preliminary Results). Code 691. NASA GSFC, March 17, 2009.
- [13] H. Noda, H. Araki, S. Goossens, Y. Ishihara, K. Matsumoto, S. Tazawa, N. Kawano, S. Sasaki, Illumination conditions at the lunar polar regions by Kaguya (Selene) Laser altimeter, *Geophys. Res. Lett.* 35 (2008) L24203. <http://dx.doi.org/10.1029/2008GL035692>.
- [14] D.B.J. Bussey, J.A. McGovern, P.D. Spudis, C.D. Neish, H. Noda, Y. Ishihara, S.-A. Sørensen, Illumination conditions of the south pole of the Moon derived using Kaguya topography, *Icarus* 208 (2010) (2010) 558–564. Elsevier.
- [15] E. Mazarico, G.A. Neumann, D.E. Smith, M.T. Zuber, M.H. Torrence, Illumination conditions of the lunar polar regions using LOLA topography, *Icarus* 211 (2) (2011) 1066–1081.
- [16] Paul Bourke, Mars—high resolution renderings from the MOLA 1/32 Degree Dataset. Website at <<http://local.wasp.uwa.edu.au/~pbourke/exhibition/mars32/>>, September 2010.
- [17] Christoph Hormann, Rendering planets. Website at <[www.ima-gico.de/pov/planets.html](http://www.ima-gico.de/pov/planets.html)>, June 2010.
- [18] T.P. McClanahan, L.G. Evans, R.D. Starr, I. Mitrofanov, Fast ray tracing of lunar digital elevation models. NASA Goddard Space Flight Center, Computer Sciences Corp. at NASA/GSFC, Catholic University at Institute for Space Research, Moscow, Russia.
- [19] Satellite tool kit: Release 9. Exton, PA. Analytical Graphics, Inc, 2010.
- [20] Global mapper software: Release 11.01. Global Mapper Software LLC Gardiner, Maine, USA. Blue Marble Geographics, 2010.
- [21] ENVI Software: Release 4.7. White Plains, N.Y., USA. I.T.T. Visual Information Solutions, 2010.
- [22] ISIS: Release 3. Reston, VA, USA. United States Geological Survey.
- [23] Kaguya (Selene) product format Description—Laser Altimeter (LALT). Version 1.0, November 1, 2009.
- [24] Selenoloical and Engineering Explorer (SELENE) data archive. Website archive at <<http://www.soac.selene.isas.jaxa.jp/archive/>>, Japan Aerospace Exploration Agency, 2011.
- [25] Grant H. Heiken, David T. Vaniman, Bevan M. French, LUNAR sourcebook—A user's guide to the Moon, Cambridge University Press, Cambridge (New York), 1991.
- [26] Kaguya HDTV video, V-044-0158, JAXA/NHK, 2008, retrieved from <[http://jda.jaxa.jp/jda/v4\\_e.php?v\\_id=70216038ee972256a bad4b95762d10d4&mode=level&time=N&genre=4&category=4064 &mission=4067](http://jda.jaxa.jp/jda/v4_e.php?v_id=70216038ee972256a bad4b95762d10d4&mode=level&time=N&genre=4&category=4064 &mission=4067)> on 2010/02/10.